Journal of Geochemical Exploration 197 (2019) 174–183

Contents lists available at ScienceDirect

Journal of Geochemical Exploration

journal homepage: www.elsevier.com/locate/gexplo

Geological and contaminant transport assessment of a low level radioactive waste disposal site

Abdel-Aal M. Abdel-Karim[a], Ahmed A. Zaki[b], Waheed Elwan[a], Mohamed R. El-Naggar[b,*], Mahmoud M. Gouda[b]

[a] Geology Department, Faculty of Science, Zagazig University, Post Code 44519, Zagazig, Egypt
[b] Hot Laboratories Center, Atomic Energy Authority, Post Code 13759, Cairo, Egypt

ARTICLE INFO

Keywords:
Red fine sand
Inshas
Geochemistry
Metal ions
Breakthrough
Modeling

ABSTRACT

The protective function of a radioactive waste disposal is provided by natural geological barrier itself. Sand and sandstone samples were taken from Inshas rad-waste disposal site and were subjected to geochemical-physical examinations. The rock volumes of such samples were composed of 70% quartz and 10% plagioclase beside 17% interstitial matter. The weathering indices indicated moderate weathering of the source materials. Provenance studies suggested the derivation from recycled quartoze sediments. The presented high contents of the interstitial Fe_2O_3 (hematite/goethite) and Al_2O_3 (clay/kaolinite) were important agents for preventing pollutants transport via adsorption and the reduced porosity (10–20%) and permeability (0.1–6 md). Flow and transport of Cs^+ and Sr^{2+} ions in groundwater was simulated using fixed bed sand column under the effect of initial ion concentration. Hights of mass transfer zones of Cs^+ testing beds and their rates of movement and fractional capacities were found to be higher than those of Sr^{2+}. The maximum adsorption capacities were calculated using Thomas and Yoon-Nelson models. The inlet concentration of both metal ions was directly related to the 50% breakthrough time. The obtained data indicated a high opportunity of Inshas area to meet the requirements posed by the International Atomic Energy Agency for shallow disposal.

1. Introduction

Low level waste is defined as a residual category for radioactive waste material that is not otherwise categorized - and has no lower or upper activity limits (Heimberg, 2016). The generated radioactive waste is divided into liquid, solid and gaseous wastes. Aqueous liquid radioactive wastes were generated during research reactor operations and in other operations involving the application of radioisotopes (e.g. medicine, research and education) (El-Naggar and Amin, 2018). Their main radiations come from β emitters such as fission products (e.g. ^{137}Cs and ^{90}Sr). Strontium-90 is one of the most hazardous radionuclides, posing a long term radiation hazard because of its long half-life (~ 29 y) and high mobility (Froidevaux et al., 2006). The half life time of cesium-137 is 30 years, its high water solubility enables it to migrate long distances (Vejsada et al., 2005). The disposal of low and intermediate levels radioactive wastes in the shallow ground is one of the options being used to provide protection for man and his environment.

The principal for disposal option includes potential sites that are evaluated on the basis of their ability to contribute to the isolation of the waste and limit radionuclide emissions to minimize potential adverse impacts on humans and the environment (IAEA, 1994). Inshas area (~1.0 Km^2; longitudes of 31° 20′ & 31° 30′ E and latitudes of 30° 15′ & 30° 25′ N) is considered as an important region for the Egyptian Atomic Energy Authority (Fig. 1a). Inshas area is exposed by quaternary deposits which represented by different formations like Inshas and Bilbies ones (Fig. 1b). The former occupies the central part of the study area that consists of cross-bedded sand, intercalated with Nile mud and silt. While the later formation is located in the northern part of the area and made up of medium to coarse grained and cross-bedded sands with plant roots and carbonate pockets (Araffa et al., 2012). Many studies on this area have carried out to evaluate its suitability for the disposal of low levels radioactive wastes (Abdel-Aziz, 1996; Abdel-Karim et al., 2016).

The multi-barriers concept that relay on using engineered barriers to augment natural barriers has been developed (Abdel-Karim et al., 2016; Abdel-Rahaman et al., 2009). Such developed studies based on the fact that radionuclides can readily adsorb to iron $^{(III)}$ (hydr)oxides, which are common minerals in soil and groundwater, such as goethite and hematite, and clay minerals (Finch and Murakami, 1999).

* Corresponding author.
E-mail address: elnaggar74@yahoo.com (M.R. El-Naggar).

https://doi.org/10.1016/j.gexplo.2018.12.011
Received 3 September 2018; Received in revised form 19 November 2018; Accepted 10 December 2018
Available online 12 December 2018
0375-6742/

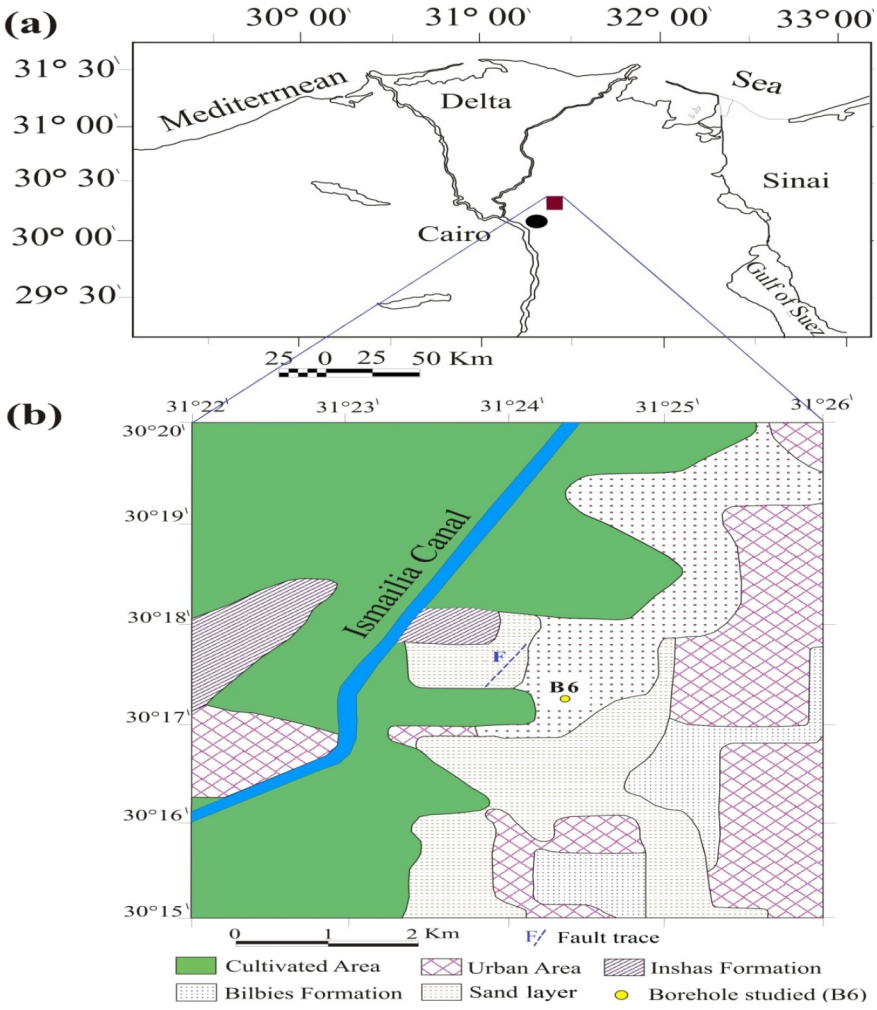

Fig. 1. Maps showing a: location and b: lithostratigraphy of the study area (Araffa et al., 2012).

Adsorption to iron-bearing minerals is favored by the high binding affinity of radionuclide ions to geosphere (Bostick et al., 2002; Duff and Amrhein, 1996; Wazne et al., 2003) due to their reactive surfaces and high specific surface areas (Schwertmann and Cornell, 2003). In this respect, a geochemical analysis was carried out by Abdel-Karim and co-workers (Abdel-Karim et al., 2016) to investigate the mineral composition of the clay samples taken from Inshas disposal site. They concluded that the adsorption capacity of Cs^{+} and Sr^{2+} onto clay sample was increased when initial metal ions concentration was increased and the increase of temperature led to decrease in the adsorption of these ions. Additionally, Zeng and co-workers stated that red (Fe oxides-rich) sandstones and sands are among the most common products of weathering of rocks that are important adsorbents for radionuclides (Zeng et al., 2009). Such importance is due to their relatively negative charge, middle specific surface area and surface hydroxyl groups which affects the fate and mobility of radioactive contaminants in the geosphere (Singh, 2010).

The studied boreholes (B_6) located in Belbies formation, consist of litho-stratigraphy succession (Fig. 2a) of quaternary and tertiary sediments arranged vertically from top to bottom as following: a) the quaternary sediments which are represented by fine ferruginous red sands and silty sand (~2 m), b) tertiary sediments which is composed of miocene compacted ferruginous fine red sand and sandstones (~5 m), clay (~1 m), fine to medium sand (~7 m) and coarse sand and sandstone (~ 12 m) (Abdel-Aziz, 1996). The general groundwater flow of the area is running from the east to the northeast direction. The absolute level of groundwater is usually 12.9 to 14.2 m above sea level which directly connected with Ismailia canal (Fig. 2b) (Araffa et al., 2012).

Thus, the present study was designed to subject representative sand samples, which were taken from Inshas low level radioactive waste disposal site, to geochemical examinations. This was carried out in order to explore the meeting between the study area and the requirements posed by IAEA for shallow disposal. In the context of achieving this goal, sand and sandstone were sampled at different depths to make: 1) petrographic studies with the associated porosity and permeability; 2) quantitative elemental analysis in order to deduce the provenance of the source rock, the degree of chemical weathering and maturity and climatic conditions during sedimentation; 3) simulation of the flow and transport of Cs^{+} and Sr^{2+} ions in groundwater through red fine sand fixed beds and 4) mathematical modeling of the breakthrough data.

2. Materials and methods

2.1. Reagents

Chloride salts of cesium and strontium were products of Sigma-Aldrich Co. Stock solutions of the tested chloride salts were prepared by dissolving the respective appropriate quantities in de-ionized water (18 MΩ/cm).

2.2. Geological sampling

Dependence on borehole No. 6 (B_6, Fig. 1b) which is located in

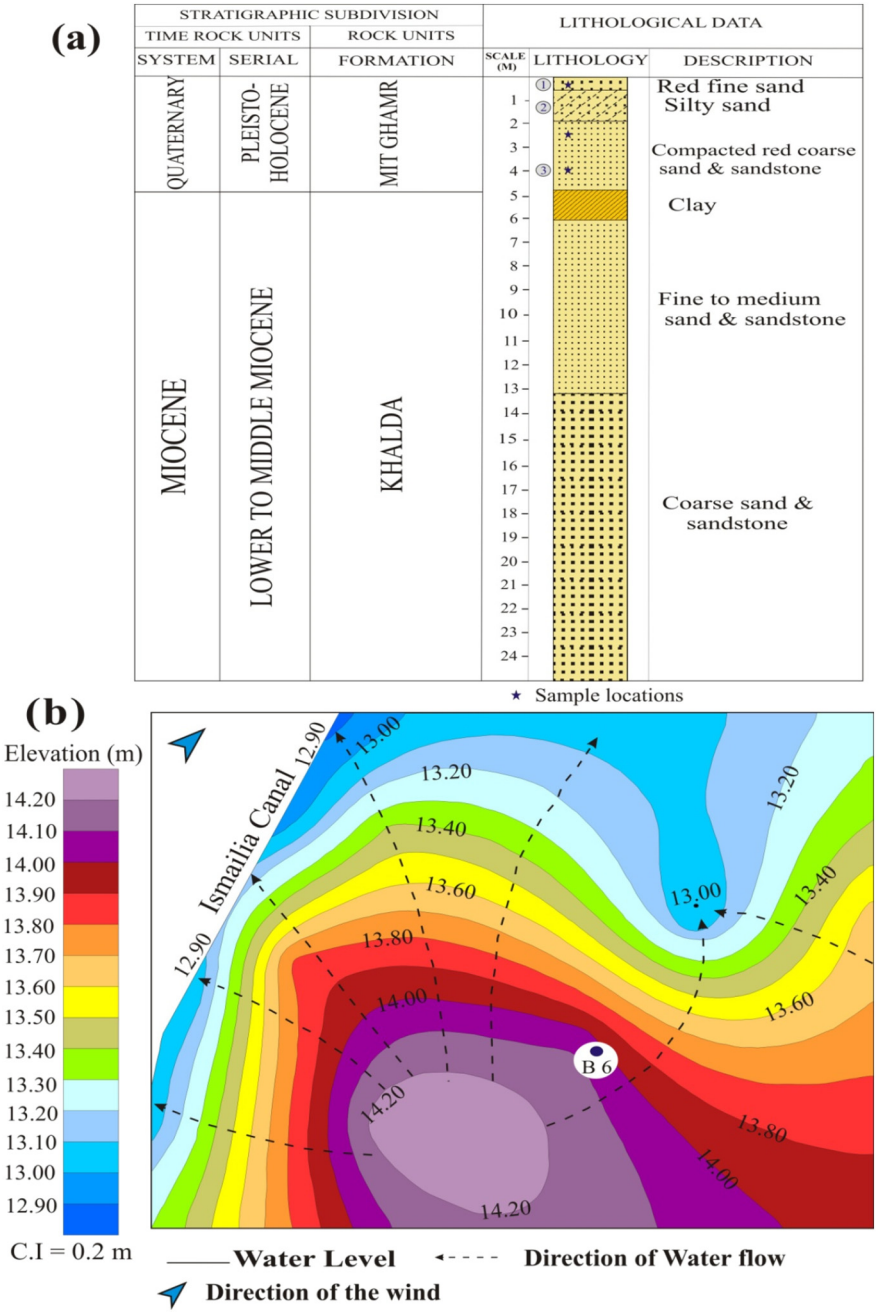

Fig. 2. a: vertical section showing the lithostratigraphy of the studied boreholes B_6 (Abdel-Aziz, 1996), b: levels and direction of the groundwater flow (Araffa et al., 2012).

Belbies formation, three samples (samples 1, 2 and 3) was withdrawn. These samples were taken at 0.4, 2.5 and 4.0 m depths representing different varieties of fine sands which are red fine sand (RFS; at 0.4 m) and compacted red coarse sand & sandstone (CRCS; at 2.5 and 4.0 m).

2.3. Characterizations

2.3.1. Physical, petrographic and geochemical analyses

The three representative samples from Inshas disposal site were physically analyzed in terms of some grain size parameters (mean grain size and sorting values). This was carried out in a Ro-Tap sieve shaker using sieves (Φ1–4.25 f at 0.50 f intervals) for 20 min. Cumulative curves were constructed and the equations of Folk and Ward (Folk and Ward, 1957) were applied. Modal mineralogical determinations were carried out using 300 grains/thin section. The point counts were done using both Gazzi-Dickinson (Gazzi, 1966; Dickinson, 1970) and standard methods. Petrographic studies have been carried out under the polarizing microscope on thin-sections. Geochemical analyses were done by the aid of X-ray fluorescence (XRF; Philips, Vacuum-Spectrograph with a Ga solution as an internal standard). Such quantitative elemental analyses were utilized to determine the provenance, maturity and climatic conditions during sedimentation, weathering of source area, and tectonic setting.

2.3.2. Physico-chemical analyses

The RFS sample was dried, crushed and sieved through the 250-μm sieve. It was characterized using X-ray diffraction (XRD; Shimadzu XD-D1), Fourier transform infrared (FT-IR; BOMEM FTIR, MB-Series) and differential thermal/thermogravimetric analyses (DTA/TGA; Shimadzu DTG-60/60H with sample holder in N_2 atmosphere).

2.4. Fixed bed column investigations

This kind of investigations allows more efficient realization of the adsorptive property of a geosystem with retardation of radio-contaminants. Unfractioned RFS sample was packed into a column of 16.0 cm height and 1.3 cm width. Different concentrations (50, 100 and 300 mg/L) of Cs^+ and Sr^{2+} aqueous solutions were prepared at pH of 7.0 ± 0.2. A high pressure pump (Nihon Seimitsu Kagaku Co. Ltd. Japan, SP-D-2502 U) was used to feed solutions into the examined fixed beds in an upward direction in order to minimize the entrapment of air bubbles. Experiments were done at constant temperature, pH value and flow rate (298 K, 7.0 ± 0.2 and 1.0 mL/min, respectively). Effluents were collected from fixed beds in known fraction volumes for atomic absorption spectroscopic analysis (Buck Scientific, VGP-210). Desorption studies of Cs^+ and Sr^{2+} from loaded fixed beds were carried out using 1.0 M HCl.

3. Results and discussion

3.1. Physical properties of sand samples

Most of the sand and sandstone of Inshas area are reddish brown colored, fine (0.10–0.25 mm) to coarse (0.5–1.5 mm) grained. The grain size distribution of the studied site shows a unimodal class that mostly in the fine to medium sand and sandstone size. Very coarse grains are sometimes observed. The grain shape exhibits sub-spherical (55%), spherical (40%) and angular (5%). The sorting of the present sedimentary layers ranges from moderate to well sorted (0.35–0.65) (Folk and Ward, 1957), which in turn was related to permeability values. Barker and Tellam suggested that sand and sandstone layers have a permeability range from 0.1 to 10 md (Barker and Tellam, 2006). However, the present studied layers of Inshas disposal site have lower permeability range (0.1–6 md) compared with the above referenced ones. This probably due to the high compaction and cementation of the rocks by red iron oxide, silica, calcite and clay which are usually reduced the porosity and permeability. This feature will decrease the possibilities of infiltration of radionuclides to reach the ground water aquifers through surface or rain water as well as a suitability of a disposal site. The petrographic studies (Fig. 3) revealed that sand and sandstone of Inshas area are composed mainly of quartz (mean 70% of rock volume), with minor amounts of plagioclase (mean 10%). The interstitial matter comprises clay matrix and cement, with a mean of 17% of rock volume. The matrix is composed of Fe-oxides (hematite, goethite), clays and quartz grains of fine silt size. In a few cases, clayey patches may represent a pseudomatrix derived from the deformation of sand-sized clay aggregates. Based on angularity, sorting and matrix content, most of sandstones are of medium mineralogical maturity. Quartz grains are varied in size, shape and habit. Some plagioclase form megacryst which exhibit lamellar twinning, glide plane and affected by micro-fault deformation (Fig. 3a). Quartz is found as large grains (Fig. 3b) or very fine fragmented grains (Fig. 3c), which grains usually exhibit wavy extinction, probably due to their deformation. It is commonly associated by Fe-oxides and clay minerals. Secondary quartz (after diagenesis) associated by clay minerals and iron oxides is recoded (Fig. 3d).

3.2. Geochemical analysis

The elemental analysis of the three sand and sandstone samples from Inshas disposal site are given in Table 1. The major oxide contents are SiO_2 (64.59–70.15 wt%), Fe_2O_3 (2.73–17.82 wt%), Al_2O_3 (3.32–6.51 wt%) and CaO (4.98–8.56 wt%). MgO, Na_2O, TiO_2, K_2O and MnO comprise minor amounts. The high contents of Fe_2O_3 and Al_2O_3 are important factors for the adsorption process of the nuclide metal ions. Mahapatra and co-workers utilized the iron oxide–alumina mixed nanocomposite as an efficient adsorbent for removal of metal ions (Mahapatra et al., 2013). It is therefore that the presence of high contents of iron oxides is more likely in controlling adsorption of Cs^+ and Sr^{2+} onto the studies sand samples. Additionally, the obtained data can be utilized to deduce the provenance of the source rock, the degree of chemical weathering and maturity and climatic conditions during sedimentation.

3.2.1. Provenance

The major elements provenance discriminant function diagram for the studied sand samples (Shaohao et al., 2016) can be obtained by:

$$\text{Discriminant function 1} = 9.09 + 0.607\,Al_2O_3 + 0.760\,Fe_2O_3 + 0.616\,CaO + 0.509\,Na_2O - 1.773\,TiO_2 - 0.50\,MgO - 1.224\,K_2O \quad (1)$$

$$\text{Discriminant function 2} = 0.445\,TiO_2 + 0.07\,Al_2O_3 + 0.438\,CaO + 1.475\,Na_2O + 1.426\,K_2O - 1.142\,MgO - 0.25\,Fe_2O_3 - 6.861 \quad (2)$$

The discriminant function diagram (Fig. 4a) indicates a quartzose sedimentary source for the studied samples. The diagram discriminates four major provenance categories of mafic, intermediate, felsic, and quartzose recycled (Sahraeyan and Bahrami, 2012).

3.2.2. Weathering in the source area

Weathering indices are useful tools to illustrate weathering profiles and establish the extent of weathering. Table 2 gives the chemical index of alteration (CIA) (Nesbitt and Young, 1982), the chemical index of weathering (CIW) (Harnois, 1988), the plagioclase index of alteration (PIA) (Fedo et al., 1995) and the mineralogical index of alteration (MIA) (Voicu et al., 1997) which were calculated by:

$$CIA = \frac{Al_2O_3}{Al_2O_3 + CaO + Na_2O + K_2O} \times 100 \quad (3)$$

$$CIW = \frac{Al_2O_3}{Al_2O_3 + CaO + Na_2O} \times 100 \quad (4)$$

$$PIA = \frac{Al_2O_3 - K_2O}{Al_2O_3 + CaO + Na_2O - K_2O} \times 100 \quad (5)$$

$$MIA = 2 \times (CIA - 50) \quad (6)$$

The average CIA and CIW values of the studied sand samples were ranged from 67.56 to 76.17% and 76.02 to 88.99%, respectively suggesting a moderate weathering either of the original source or during transport before deposition (Voicu and Bardoux, 2002; Harnois, 1988). This may be associated with complete removal of alkali and alkaline earth elements and an increase of Al_2O_3 contents (Fedo et al., 1995; Dupuis et al., 2006). According to Voicu and co-workers, the MIA values can be subdivided into incipient (0–20%), weak (20–40%), moderate (40–60%) and intense to extreme (60–100%) alteration (Fedo et al., 1995). The investigated sand sample display MIA average values of 44, indicating moderate alteration of these samples. The plot of CIA versus Al_2O_3 depicts that most samples of moderate degree of weathering for the source materials (Fig. 4c). The degree of the chemical weathering was estimated using the PIA. To be ranged from 74.79 to 84.22% (Average ~ 81%) for Inhas disposal site indicating again, a moderate weathering for the source.

3.3. Mineralogical, infra-red and thermal analyses

Fig. 5 shows different phases which are present in Inshas RFS sample and their vibrational frequencies as well as thermal stability. Fig. 5a revealed that the main mineralogical composition was quartz (20.80°, 26.67°, 50.20° 2θ, 36.54°, and 60.03°), hematite and goethite (54.28° and 64.14°, respectively) and calcite (39.4°) (Maurice, 1988).

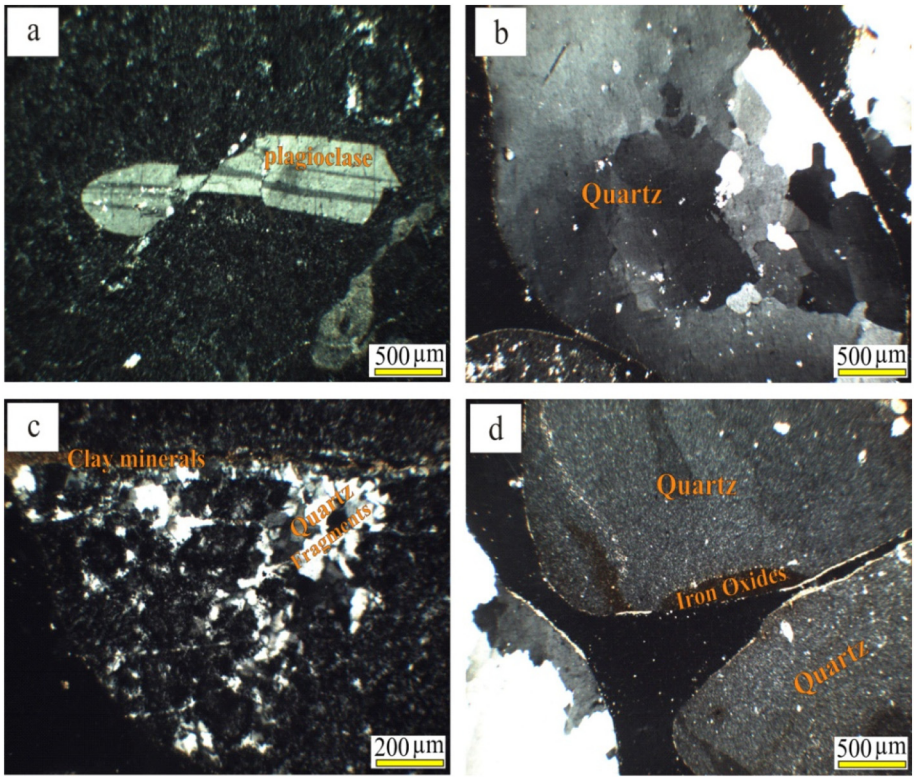

Fig. 3. Photomicrograph showing a: Occurrence of plagioclase megacryst which shows glide plane and affected by micro-fault deformation, b: Large quartz grain which shows wavy extinction, c: Fine-grained fragments of quartz and clay minerals and d: Secondary coarse grained quartz (after diagenesis) associated by clay minerals and iron oxides.

Table 1
Quantitative elemental analysis (wt., %) of different sand samples from Inshas disposal site.

Index	Red fine sand (RFS)	Compacted red coarse sandstone (CRCS)	
	Sample no. 1 (0.4 m depth)	Sample no. 2 (2.5 m depth)	Sample no. 3 (4.0 m depth)
Na_2O	0.32	0.33	0.20
MgO	1.01	6.52	6.65
Al_2O_3	6.51	3.32	5.12
SiO_2	64.59	75.71	70.16
K_2O	0.93	0.20	1.69
CaO	4.98	8.56	7.79
TiO_2	0.44	0.07	0.13
Cr_2O_3	0.07	0.01	0.06
MnO	0.23	0.04	0.07
Fe_2O_3	17.82	2.73	4.53
Cl	0.1	0.16	0.29
LOI	3.00	2.35	3.31

LOI: Loss of Ignition.

The presences of Fe (hydr)oxide (hematite and goethite) and clay minerals as diagenetic and alteration products within the sand and sandstone samples decrease their permeability. They also may responsible for the most of adsorptive behavior. FT-IR spectrum (Fig. 5b) showed the presence of sharp peak, with high intensity, at 1036 and 1086 cm^{-1} which may be due to stretching vibrations of Si—O—Si and Si—O—Al, respectively (El-Naggar, 2014). The band arising at 445 cm^{-1} was assigned to bending vibrations of O—Si—O (El-Naggar et al., 2013). The recorded bands at 668 and 695 cm^{-1} were assigned to the symmetric stretching vibrations of Si—Al—O. The assignment at 794 cm^{-1} can be attributed to the stretching vibrational modes of O—T—O (T = Si or Al) (Pacakova et al., 2000). Assignments around 3400 and 1600 cm^{-1} may be due to the bending vibrations of water which is physically bonded to the aluminol and/or silanol groups (Dimas et al., 2009; El-Naggar and El-Dessouky, 2017). The observed band at 1421 cm^{-1} representing the vibration of the calcite and as a characteristic doubly degenerate asymmetric stretching, CO_3 (C═O) (El-Naggar and Amin, 2018). In the TGA/DTA curves (Fig. 5c), a first continuous mass loss (about 1.06%) is observed at temperature up to 150 °C, which may be due to removal of external water molecule. Also, there are endothermic peak at 574 °C with loss of mass about 1.86%. At higher temperature, the sand sample is stable with the total mass loss, which was 2.81% up to > 1000 °C.

3.4. Fixed bed column investigations

3.4.1. Effect of metal ion concentration

The breakthrough curves of different concentrations of Cs^+ and Sr^{2+} adsorbed onto water saturated sand column are shown in Fig. 6. They defined as the ratio between effluent and influent concentrations (C/C_o) vs. effluent volume (V_{eff}, mL) using a bed depth of 16.0 cm at a flow rate of 1.0 mL/min. At the influent concentration of 50.0 mg/L, the breakthrough (exhaustion) time was 28.17 and 20.0 h (1690 and 1200 mL) for Cs^+ and Sr^{2+}, respectively. By increasing the influent concentration to 300.0 mg/L, faster exhaustion times were brought at 13.17 and 11.5 h (790 and 690 mL) shifting breakthrough curves to the left, for Cs^+ and Sr^{2+}, respectively. This notice may be due to the positive relationship between the diffusion and mass transfer coefficients and the gradient's concentration (Uddin et al., 2009). Integration of adsorbed ion concentration (C_{sor}, mg/L) at a given flow rate (F, mL/min.) versus time gives the area under the breakthrough curve which in turn gives the total adsorbed amount of ions ($Q_{tot,s}$, mg):

$$Q_{tot,S} = \frac{F}{10^3}\int_{t=0}^{t=tot} C_{sor}\,dt = \frac{F}{10^3}\int_{t=0}^{t=tot} (C_{in} - C_{eff})dt \quad (7)$$

The total fed amount of ions (X, mg) and column performance (CP, %) were calculated by Eqs. (8) & (9), respectively, where V_{eff} is the effluent volume (ml).

$$X = \frac{C_{in} V_{eff}}{10^3} \quad (8)$$

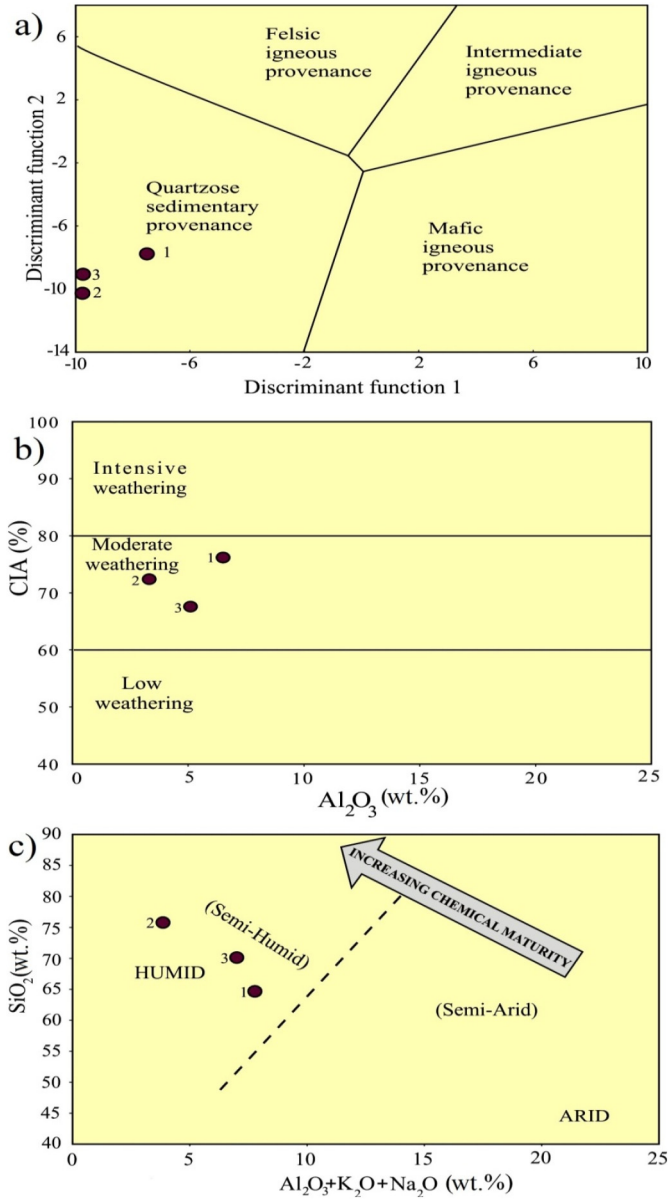

Fig. 4. Geochemistry of the analyzed clay showing a: Provenance discriminant function diagram for the studied samples after Shaohao and co-workers (Shaohao et al., 2016) and Sahraeyan & Bahrami (Sahraeyan and Bahrami, 2012), b: Chemical index of alteration (CIA) versus Al_2O_3 and c: Chemical maturity expressed by SiO_2 versus Al_2O_3 + K_2O + Na_2O after Suttner & Dutta (Suttner and Dutta, 1986).

Table 2
Weathering and alteration indices of the Inshas disposal site sand samples.

Index	Red fine sand (RFS)	Compacted red coarse sandstone (CRCS)	
	Sample no. 1 (0.4 m depth)	Sample no. 2 (2.5 m depth)	Sample no. 3 (4.0 m depth)
CIA	76.17	72.48	67.56
PIA	84.22	74.79	83.88
CIW	86.32	76.02	88.99
MIA	52.34	44.96	35.12

$$CP = \frac{Q_{tot,S}}{X} \times 100 \tag{9}$$

At the given experimental conditions, the total fed and adsorbed amounts of ions, column performance and bed capacity were calculated and given in Table 3.

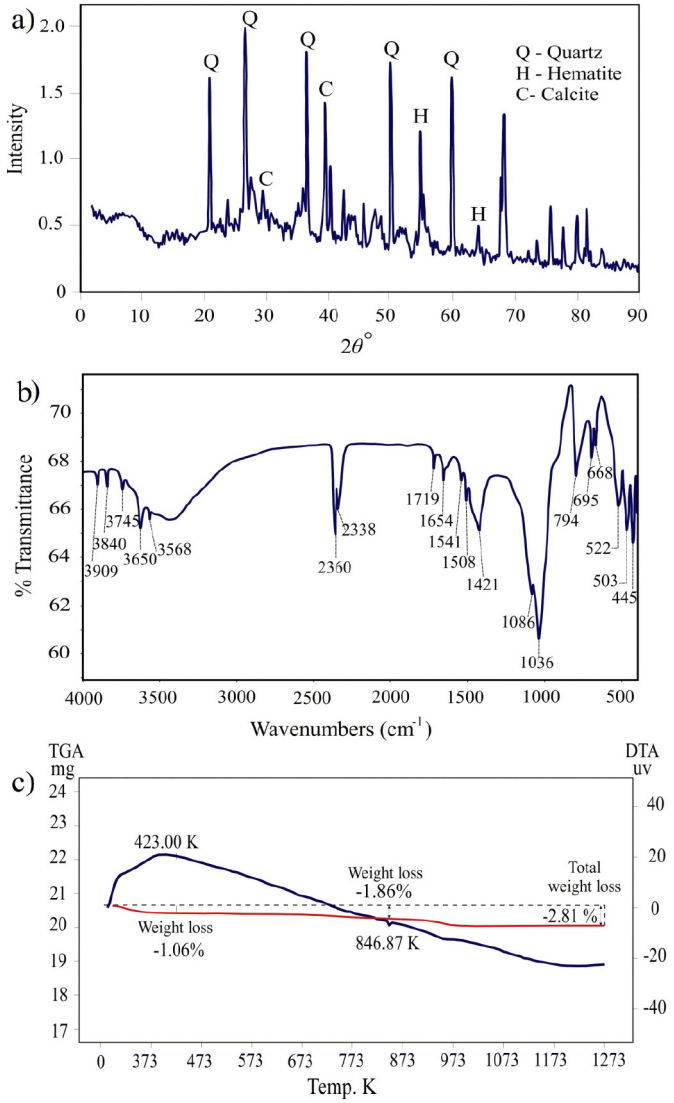

Fig. 5. Characterization of the red fine sand (BFS) sample showing a: X-ray diffraction, b: FT-IR spectrum and c: TGA/DTA curves.

3.4.2. Analysis of mass transfer zone (MTZ)

This zone suggests where adsorption was practically took place along the examined fixed bed (Naddafi et al., 2007). The developed performance of a fixed bed directly affects on the shape of the MTZ and consequently its height (H_{MTZ}, cm) which can be calculated using:

$$H_{MTZ} = \frac{h(t_e - t_b)}{t_b + F_c(t_e - t_b)} \tag{10}$$

where h is the height of the fixed bed (cm); t_e is the exhaustion time (min); t_b is the breakthrough time (cm) and F_c is the factional capacity. Within a MTZ, F_c is defined as the ratio between the quantity of the adsorbed metal ion and the potential elimination capacity of an adsorbent and can be obtained by Eq. (11) (Mahendra et al., 2015):

$$F_c = \frac{\int_{t_b}^{t_e} (C_{in} - C_{eff})dt}{C_{in}(t_e - t_b)} \tag{11}$$

The rate of movement of a MTZ (U_z, cm/min) is a function of the adsorption capacity of a fixed bed and is directly related to H_{MTZ} by:

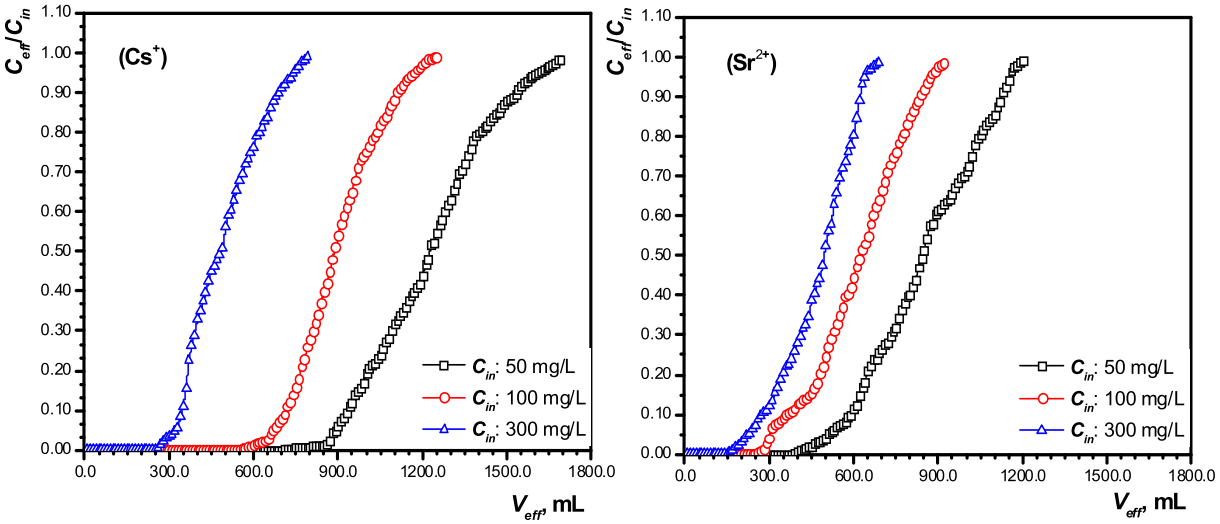

Fig. 6. Effect of metal ion concentration on the breakthrough curves of Cs^+ and Sr^{2+} adsorbed onto Inshas disposal site sand column. (pH, 7.0 ± 0.2; bed depth, 16.0 cm; bed width, 1.3 cm; influent flow rate, 1.0 mL/min.; ambient temperature).

Table 3
Effect of Cs^+ and Sr^{2+} influent concentration on breakthrough capacity of Inshas disposal site sand column.

Metal ion	C_{in}, mg/L	X, mg	$Q_{tot_{ss}}$, mg	CP, %	Bed capacity, mg/g
Cs^+	50	83.66	60.41	72.22	2.28
	100	124.74	89.80	71.99	3.39
	150	250.00	158.11	63.24	5.97
Sr^{2+}	50	58.41	41.77	71.51	1.58
	100	105.65	74.11	70.21	2.80
	150	167.00	104.51	62.58	3.94

$$U_Z = \frac{H_{MTZ}}{t_Z} = \frac{H_{MTZ}}{t_e - t_b} \tag{12}$$

where t_Z (min) is the time required for the movement of a MTZ down its own length. The percentage of saturation of the column is given by:

$$\%Saturation = \frac{h + (F_c - 1)H_{MTZ}}{h} \times 100 \tag{13}$$

Data in Table 4 indicated that the heights of MTZ were decreased by increasing the initial metal ions concentration indicating faster adsorption at high concentration gradients. The F_c, H_{MTZ} and U_Z regarding Sr^{2+} were higher than those of Cs^+ reflecting more adsorption sites available for adsorption of the former than the later ion. The smallest ionic radius of Sr^{2+} (0.112 nm) compared to Cs^+ (0.167 nm) (Daniels and Alberty, 1966) may be responsible for passing Sr^{2+} quit readily through more active sites than Cs^+.

3.5. Mathematical description

3.5.1. Thomas model

When a fixed bed column is designed the maximum adsorption capacity is needed to be assessed. Here, Mathematical modeling of the breakthrough data is a suitable tool to gain information about transport of contaminants along the naturally designed Inshas sand columns. Thomas model (Thomas, 1944) is widely applied in this concern assuming the Langmuir isotherm and the reversible 2nd-order reaction kinetics Eq. (14).

$$\frac{C_{eff}}{C_{in}} = \frac{1}{1 + \exp(K_{Th} q_{o_{Th}} m/F - K_{Th} C_{in} t)} \tag{14}$$

where K_{Th} and $q_{o_{Th}}$are Thomas's rate constant (mL/min mg) and its maximum adsorption capacity (mg/g), respectively. While m and F are mass of the sand bed (g) and flow rate (mL/min), respectively. By the aid of the linear expression of Thomas model [Eq. (15)] the model parameters can be computed by plotting $ln(C_{in}/C_{eff} - 1)$ vs. t (Fig. 7).

$$ln\left(\frac{C_{in}}{C_{eff}} - 1\right) = \frac{K_{Th} q_o m}{F} - K_{Th} C_{in} t \tag{15}$$

Data in Table 5 revealed comparable values of Thomas's rate constant (K_{Th}) for both metal ions which were linked to the metal ion concentration with an inverse relationship. The maximum adsorption capacities of the designed sand columns were calculated theoretically ($q_{o_{Th}}$). It was found to be close to the experimentally obtained ones. These findings reflected the applicability of Thomas model to describe the presented adsorption processes which may be due to extremely small resistances of the internal and internal diffusion along the fixed bed (Aksu and Gönen, 2004). Such small resistances can be considered as acceptable phenomena regarding the radioactive waste disposal purposes.

3.5.2. Yoon-Nelson model

The basic assumption of this model (Yoon and Nelson, 1984) related

Table 4
Parameters of mass transfer zones of Cs^+ and Sr^{2+} adsorbed onto Inshas disposal site sand column, as affected by metal ion concentration.

Metal ion	C_{in}, mg/L	t_e, min.	t_b, min.	t_Z, min.	F_c	H_{MTZ}, cm	U_Z, cm/min.	Saturation, %
Cs^+	50	1650	850	800	0.432	10.70	0.013	61.55
	100	1200	620	580	0.516	10.09	0.017	69.09
	300	610	290	320	0.730	9.78	0.031	83.27
Sr^{2+}	50	1180	430	750	0.569	15.01	0.019	61.79
	100	870	310	560	0.599	13.88	0.025	64.80
	300	630	210	420	0.719	13.13	0.031	76.63

(pH, 7.0 ± 0.2; bed depth, 16.0 cm; bed width, 1.3 cm; influent flow rate, 1.0 mL/min.; ambient temperature)

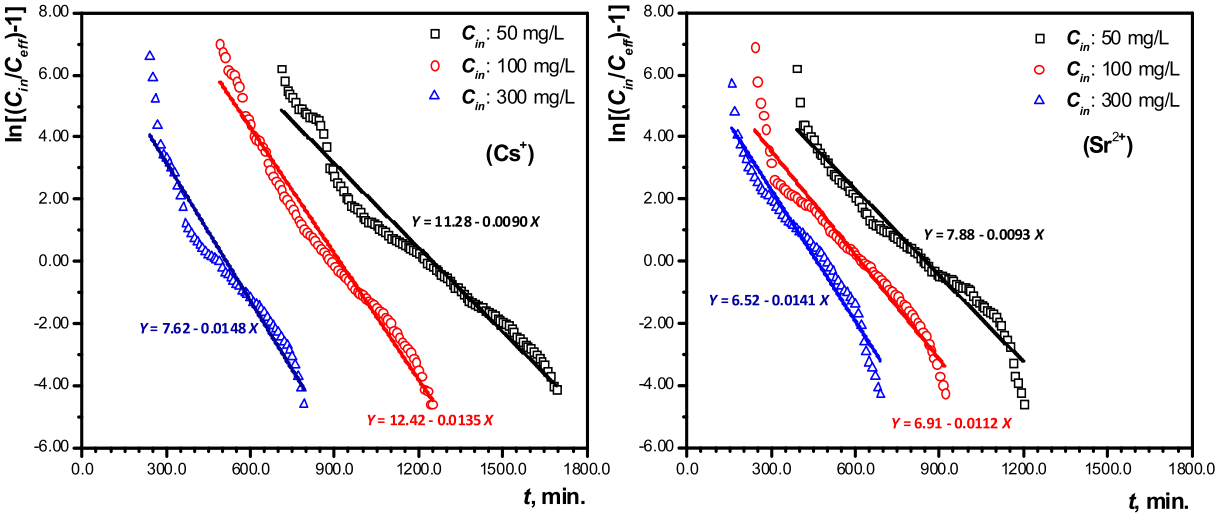

Fig. 7. Thomas modeling of the breakthrough data of Cs^+ and Sr^{2+} adsorbed onto Inshas disposal site sand column, as affected by metal ion concentration. (pH, 7.0 ± 0.2; bed depth, 16.0 cm; bed width, 1.3 cm; influent flow rate, 1.0 mL/min.; ambient temperature).

the decrease in the probability of an adsorbate to be adsorbed to its breakthrough and adsorption onto an adsorbent. Regarding a single component system, it can be expressed by Eq. (16) in which K_{YN} and τ are the Yoon-Nelson's rate constant (min^{-1}) and the time required for 50% adsorbate breakthrough (min), respectively.

$$\frac{C_{eff}}{C_{in} - C_{eff}} = exp(K_{YN}t - \tau K_{YN}) \quad (16)$$

The Yoon-Nelson model parameters can be computed according to its linear form given in Eq. (17) by plotting ln $[C_{eff}/(C_{in}\text{-}C_{eff})]$ vs. t (Fig. 8).

$$ln\left(\frac{C_{eff}}{C_{in} - C_{eff}}\right) = K_{YN}t - \tau K_{YN} \quad (17)$$

Accordingly, the quantities of the adsorbed metal ions ($q_{o_{YN}}$, mg/g) can be calculated by:

$$q_{o_{YN}} = \frac{C_{in}F\tau}{m} \quad (18)$$

Data given in Table 5 indicated that increasing in the inlet concentration of both Cs^+ and Sr^{2+} led to an increasing in the Yoon-Nelson rate constant (K_{YN}) which associated with an decreasing in the 50% breakthrough time (τ). Also, it was observed that lower concentrations gave better fitting than higher ones indicating the applicability of Yoon-Nelson model to describe adsorption of low concentrations of Cs^+ and Sr^{2+} onto Inshas sand column.

3.6. Adsorption-desorption studies

The adsorption and desorption characteristics of Cs^+ and Sr^{2+} ions in soil and/or groundwater systems are very important with respect to environmental pollution. The adsorption-desorption studies of Cs^+ and Sr^{2+} ions onto/from Inshas sand column were carried out Fig. 9. The total amounts of adsorbed ($Q_{tot_{,S}}$, mg) and desorbed ($Q_{tot_{,D}}$, mg) Cs^+ and Sr^{2+} were calculated by integrating the area above the breakthrough curves and the area beneath the displacement curves, respectively. Such amounts beside the desorption percentage were given in Table 6.

4. Conclusion

The protective function of a radioactive waste disposal is provided by natural geological barrier itself, which is selected in such a way that its low permeability and stability characteristics should prevent contamination from reaching the biosphere. In this regard, a primary concern is the contamination of groundwater which is considered a very important vector for pollution. Nevertheless, conclusion remarks of a natural geological barrier of Inshas area can be summarized as following:

- Most of the sand and sandstone of radioactive waste disposal site at Inshas area were reddish brown colored with grain size distribution showing a unimodal class that mostly in the fine to medium grained. Shapes of grains exhibited sub-spherical (55%), spherical (40%) and angular (5%) types. The sorting of the present sedimentary layers ranged from moderate to well sorted which was associated with lower permeability range (0.1–6 md).

Table 5
Parameters of Thomas and Yoon-Nelson models to describe the adsorption of Cs^+ and Sr^{2+} onto Inshas disposal site sand column, as affected by metal ion concentration.

Metal ion	C_{in}, mg/L	$q_{o_{exp}}$ mg/g	Thomas model parameters			Yoon-Nelson model parameters			
			K_{Th}, mL/min mg	$q_{o_{Th}}$, mg/g	R^2	K_{YN}, min^{-1}	τ, min	$q_{o_{YN}}$, mg/g	R^2
Cs^+	50	2.28	0.181	2.358	0.965	9.0 E-3	1253.24	2.358	0.972
	100	3.39	0.134	3.464	0.975	1.35 E-2	917.90	3.466	0.981
	300	5.97	0.049	5.829	0.961	1.48 E-2	513.63	5.931	0.950
Sr^{2+}	50	1.58	0.185	1.604	0.960	9.3 E-3	846.91	1.604	0.969
	100	2.80	0.112	2.328	0.952	1.12 E-2	616.92	2.328	0.950
	300	3.94	0.047	5.235	0.955	1.41 E-2	462.51	5.243	0.951

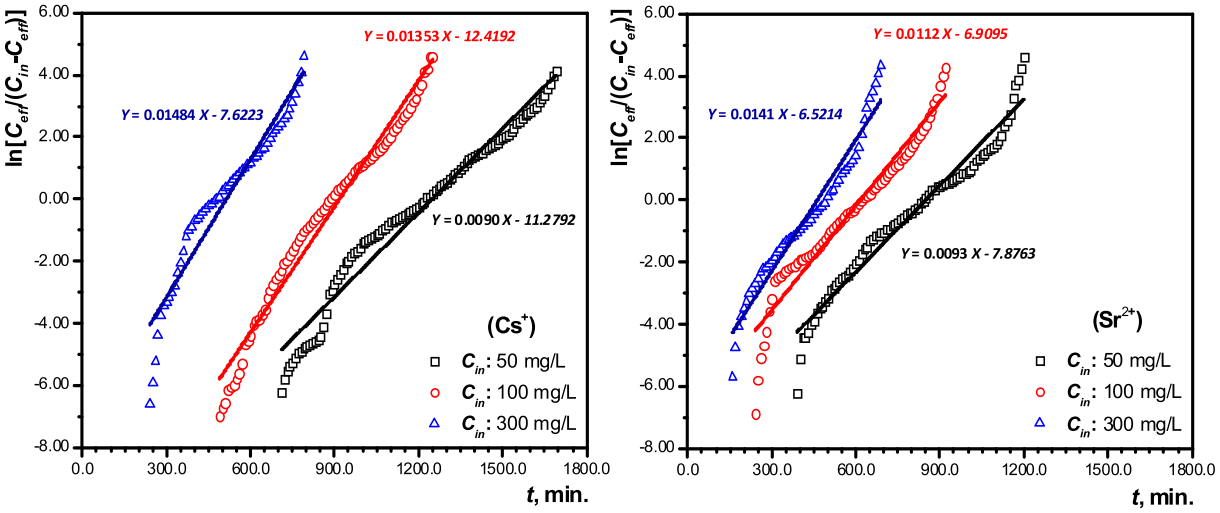

Fig. 8. Yoon-Nelson modeling of the breakthrough data of Cs^+ and Sr^{2+} adsorbed onto Inshas disposal site sand column, as affected by metal ion concentration. (pH, 7.0 ± 0.2; bed depth, 16.0 cm; bed width, 1.3 cm; influent flow rate, 1.0 mL/min.; ambient temperature).

- According to the petrographic examinations, the rock volumes of the representative sand samples were composed of 70% quartz, 10% plagioclase and 17% interstitial matter. In the major cases, the latter percent was composed of iron oxides, clays and quartz of fine silt size. While in few cases, a pseudo-matrix, derived from the deformation of sand-sized clay aggregates, may be represented.
- Quartz grains were varied in size, shape and habit. They were found as large grains or very fine fragmented ones exhibiting wavy extinction. After the diagenesis, secondary quartz which associated by clay minerals and iron oxides was recorded.
- Under the effect of the micro-fault deformation of Inshas area, some plagioclase can form megacryst exhibiting glide planed- lamellar twinning.
- Samples were subjected to geochemical analysis. Their major oxide contents were SiO_2, CaO, Al_2O_3 and Fe_2O_3, respectively. The provenance of the source rock, the degree of chemical weathering and maturity and climatic conditions during sedimentation were deduced from elemental analysis data to be of quartzose sedimentary source, of moderate weathering and of moderate alteration, respectively.
- The red fine sand sample was characterized by means of X-ray diffraction, Fourier transform infrared and thermal analyses. The XRD data revealed that the main mineralogical composition was quartz (20.80°, 26.67°, 50.20° 2θ, 36.54°, and 60.03°), hematite and goethite (54.28° and 64.14°, respectively) and calcite (39.4°). The bond vibrations of T—O—T, O—T—O (where T = Si or Al) and the physically bonded water to aluminol and/or silanol groups were assigned using FT-IR. DTA/TGA results reflected the thermal stability of the examined red fine sand sample.
- Breakthrough curves for the adsorption of Cs^+ and Sr^{2+} onto the red fine sand of Inshas disposal site were constructed, at ambient

Table 6
Total adsorbed and desorbed amounts of Cs^+ and Sr^{2+} ions onto/from Inshas sand column at different metal ion concentrations.

Metal ion	C_{in}, mg/L	$Q_{tot,s}$, mg	$Q_{tot,D}$, mg	Desorption, %
Cs^+	50	60.41	8.05	13.33
	100	89.80	25.02	27.86
	300	147.20	104.56	70.65
Sr^{2+}	50	41.77	8.26	19.77
	100	60.62	23.45	38.68
	300	139.47	87.71	62.89

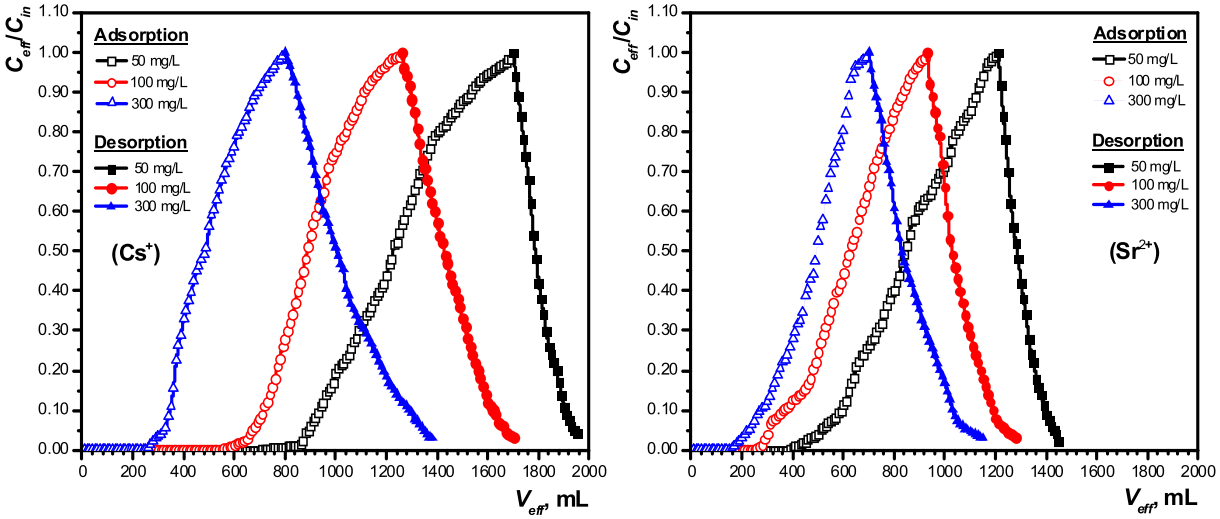

Fig. 9. Adsorption-desorption curves of Cs^+ and Sr^{2+} onto/from Inshas sand column at different metal ion concentrations. (Desorption: influent 1.0 M HCl at flow rate of 1.0 mL/min.; ambient temperature).

temperature. Effect of metal ions concentration (50–300 mg/L) was explored at constants of influent flow rate (1.0 mL/min.), bed depth (16.0 cm) and bed width (1.3 cm). Data revealed that by increasing the influent concentration to 300.0 mg/L, faster exhaustion times were brought at 13.17 and 11.5 h, compared to 28.17 and 20.0 h for 50 mg/L, shifting thebreakthrough curves to the left side, for Cs^{+} and Sr^{2+} respectively. Additionally, the total fed and adsorbed amounts, columns performance as well as beds capacity were calculated.

- Mass transfer zones were examined in terms of their heights (cm), the exhaustion times (min), the breakthrough times (cm), the factional capacities and the rates of movement of MTZs (cm/min). The heights of MTZs were decreased by increasing the initial metal ions concentration indicating faster adsorption at high concentration gradients. Hights of MTZs of Cs^{+} testing beds and their rates of movement and fractional capacities were found to be higher than those of Sr^{2+}.
- The experimentally obtained adsorption data were analyzed using Thomas and Yoon-Nelson models. The maximum adsorption capacities of the designed sand columns were calculated theoretically using the two examined models and were found to be close to the experimentally obtained ones. Increasing the inlet concentration of both metal ions led to an increasing in the Yoon-Nelson rate constant which associated with a decreasing in the 50% breakthrough time.
- The adsorption-desorption studies of both metal ions onto/from Inshas red fine sand columns were carried out using 1.0 M HCl at constant influent flow rate of 1.0 mL/min. Cesium ions were observed to be easily desorbed faster than strontium ones recording the desorption ranges from 70.65 to 13.33% and from 62.89 to 19.77%, respectively.

Acknowledgments

Authors are acknowledged stuff members of both of Radioactive Waste Management Department, Hot Lab. Center, Egyptian Atomic Energy Authority and Geology Department, Faculty of Science, Zagazig University.

References

Abdel-Aziz, M.A., 1996. Site Assessment for Disposal of Low and Intermediate Levels Radioactive Wastes Inshas Area (Ph.D. Thesis). Ain Shams University.
Abdel-Karim, A.M., Zaki, A.A., Elwan, W., El-Naggar, M.R., Gouda, M.M., 2016. Experimental and modeling investigations of cesium and strontium adsorption onto clay of radioactive waste disposal. Appl. Clay Sci. 132-133, 391–401.
Abdel-Rahaman, R.O., Ibrahim, H.A., Abdel-Moniem, N.M., 2009. Long-term performance of zeolite Na A-X blend as backfill material in near surface disposal vault. J. Chem. Eng. 149, 143–152.
Aksu, Z., Gönen, F., 2004. Biosorption of phenol by immobilized activated sludge in a continuous packed bed: prediction of breakthrough curves. Process Biochem. 39 (5), 599–613.
Araffa, S.A.S., Santos, F.A.M., Hamed, T.A., 2012. Delineating active faults by using integrated geophysical data at northeastern part of Cairo, Egypt. NRIAG J. Astron. Geophys. 1 (2012), 33–44.
Barker, R.D., Tellam, J.H., 2006. Fluid flow and solute movement in sandstones: the onshore UK Permo-Triassic red bed sequence. Geol. Soc. Lond., Spec. Publ. 263, 1–48.
Bostick, B.C., Fendorf, S., Barnett, M.O., Jardine, P.M., Brooks, S.C., 2002. Uranyl surface complexes formed on subsurface media from DOE facilities. Soil Sci. Soc. Am. J. 66 (1), 99–108.
Daniels, F., Alberty, R., 1966. Physical Chemistry, 3rd ed. Willy, New York, pp. 134.
Dickinson, W.R., 1970. Interpreting detrital modes of greywacke and arkose. J. Sediment. Petrol. 40, 695–707.
Dimas, D., Giannopoulou, I., Panias, D., 2009. Polymerization in sodium silicate solution: a fundamental process in geopolymerization technology. J. Mater. Sci. 44, 3719–3730.
Duff, M.C., Amrhein, C., 1996. Uranium(VI) adsorption on goethite and soil in carbonate solutions. Soil Sci. Soc. Am. J. 60, 1393–1400.
Dupuis, C., Hebert, R., Cote, V.D., 2006. Geochemistry of sedimentary rocks melange and flysch units south of the Yarlung Zangbo suture zone, southern Tibet. J. Asian Earth Sci. 26, 489–508.
El-Naggar, M.R., 2014. Applicability of alkali activated slag-seeded Egyptian Sinai kaolin for the immobilization of ^{60}Co radionuclide. J. Nucl. Mater. 447, 15–21.
El-Naggar, M.R., Amin, M., 2018. Impact of alkali cations on properties of metakaolin and metakaolin/slag geopolymers: Microstructures in relation to sorption of ^{134}Cs radionuclide. J. Hazard. Mater. 344, 913–924.
El-Naggar, M.R., El-Dessouky, M.I., 2017. Re-use of waste glass in improving properties of metakaolin-based geopolymers: Mechanical and microstructure examinations. Constr. Build. Mater. 132, 543–555.
El-Naggar, M.R., Aglan, R.F., Sayed, M.S., 2013. Direct incorporation method for the synthesis of molybdophosphate/MCM-41 silica composite: Adsorption study of heavy metals from aqueous solutions. J. Environ. Chem. Eng. 1, 516–525.
Fedo, C.M., Nesbitt, H.W., Young, G.M., 1995. Unraveling the effects of potassium metasomatism in sedimentary rock sand paleosols, with implications for paleoweathering conditions and provenance. Geology 23, 921–924.
Finch, R., Murakami, T., 1999. Systematics and paragenesis of uranium minerals. In: Burns, P.C., Finch, R. (Eds.), Uranium: Mineralogy, Geochemistry and the Environment. 38. Mineralogical Society of America, Washington, DC, pp. 91–180.
Folk, R.L., Ward, W.C., 1957. Brazos River bar, a study in the significance of grain-size parameters. J. Sediment. Petrol. 27 (1), 3–26.
Froidevaux, P., Geering, J., Valley, J., 2006. ^{90}Sr in deciduous teeth from 1950 to 2002: the Swiss experience. Sci. Total Environ. 367, 596–605.
Gazzi, P., 1966. Les arenarie del flysch sopracretaceo dell'Appennino modensese: correlazioni conil flysch di Monghidoro. Mineral. Petrogr. Acta 12, 69–97.
Harnois, L., 1988. The CIW index: a new chemical index of weathering. Sediment. Geol. 55, 319–322.
Heimberg, J., 2016. Low level radioactive waste management and disposition: background and information. In: Workshop Held in Nuclear and Radiation Studies Board National Academies of Sciences, Engineering, and Medicine. 15.
International Atomic Energy Agency, 1994. Considerations in the Development of Near Surface Repositories for Radioactive Waste. IAEA-TRS-417. (Vienna).
Mahapatra, A.B., Mishra, G., Hota, G., 2013. Electrospun Fe_2O_3-Al_2O_3 nanocomposite fibers as efficient adsorbent for removal of heavy metal ions from aqueous solution. J. Hazard. Mater. 258–259, 116–123.
Mahendra, C., Sathya, S.P.M., Anand, B.C., Revathy, K., Rajan, K.K., 2015. Analysis and modeling of fixed bed sorption of cesium by AMP-PAN. J. Environ. Chem. Eng. 3, 1546–1554.
Maurice, T., 1988. Techniques in Sedimentology. University of Durham, UK, pp. 393.
Naddafi, K., Nabizadeh, R., Saeedi, R., Mahvi, A.H., Vaezi, F., Yaghmaeian, K., Ghasri, A., Nazmara, S., 2007. Biosorption of lead $^{(II)}$ and cadmium $^{(II)}$ by proto-nated Sargassum glaucescens biomass in a continuous packed bed column. J. Hazard. Mater. 147 (3), 785–791.
Nesbitt, H.W., Young, G.M., 1982. Early Proterozoic climates and plate motions inferred from major element chemistry of lutites. Nature 299, 715–717.
Pacakova, V., Pockevicite, D., Armalis, S., Stulik, K., Li, J., Vasely, J., 2000. A study of the distribution of lead, cadmium and copper between and kaolin, bentonite and river sediment. J. Environ. Monit. 2, 187–191.
Sahraeyan, M., Bahrami, M., 2012. Geochemistry of sandstones from the Aghajari formation, folded Zagros Zone, southwestern Iran, implication for paleoweathering condation, provenance, and tectonic setting. Int. J. Basic Appl. Sci. 1 (4), 390–407.
Schwertmann, U., Cornell, R.M., 2003. The Iron Oxides: Structure, Properties, Reactions, Occurrences and Uses, Second ed. Wiley-VCH, New York.
Shaohao, Z., Chuanjun, W., Deru, X., Qiang, S., Xiaowen, Z., Pete, H., Maozhou, H., 2016. Provenance and depositional setting of Lower Silurian siliciclastic rocks on Hainan Island, South China: implications for a passive margin environment of South China in Gondwana. J. Asian Earth Sci. 123, 243–262.
Singh, A., 2010. Geochemical Conditions Affecting Uranium (VI) Fate and Transport in Soil and Groundwater in the Presence of Phosphate. Washington Univ., St. Louis. Missouri, pp. 201. (Thesis). http://openscholarship.wustl.edu/etd/324.
Suttner, L.J., Dutta, P.K., 1986. Alluvial sandstone composition and paleoclimate framework mineralogy. J. Sediment. Petrol. 56, 329–345.
Thomas, H.C., 1944. Heterogeneous ion exchange in a flowing system. J. Am. Chem. Soc. 66 (1664–1466).
Uddin, M.T., Rukanuzzaman, M., Khan, M.M.R., Islam, M.A., 2009. Adsorption of methylene blue from aqueous solution by jackfruit (*Artocarpus heteropyllus*) leaf powder: a fixed-bed column study. J. Environ. Manag. 90, 3443–3450.
Vejsada, J., Jelinek, E., Randa, Z., Hradil, D., Prikryl, R., 2005. Sorption of cesium on smectite-rich clays from the Bohemian Massif (Czech Republic) and their mixtures with sand. J. Appl. Radiat. Isot. 62, 91–96.
Voicu, G., Bardoux, M., 2002. Geochemical behaviour under tropical weathering of the Barama-Mazaruni greenstone belt at Omai gold mine, Guiana Shield. Appl. Geochem. 17, 321–336.
Voicu, G., Bardoux, M., Harnois, L., Grepeau, R., 1997. Lithological and geochemical environment of igneous and sedimentary rocks at Omai gold mine, Guyana, South America. Explor. Min. Geol. 6, 153–170.
Wazne, M., Korfiatis, G.P., Meng, X.G., 2003. Carbonate effects on hexavalent uranium adsorption by iron oxyhydroxide. Environ. Sci. Technol. 37 (16), 3619–3624.
Yoon, Y.H., Nelson, J.H., 1984. Aplication of gas adsorption kinetics. I. A theoretical model for respirator cartridge service time. Am. Ind. Hyg. Assoc. J. 45, 509–516.
Zeng, H., Singh, A., Basak, S., Ulrich, K.U., Sahu, M., Biswas, P., Catalano, J.G., Giammar, D.E., 2009. Nanoscale size effects on Uranium$^{(VI)}$ adsorption to hematite. Environ. Sci. Technol. 43 (5), 1373–1378.